Discovery of a novel low-cost medium-entropy stainless steel with exceptional mechanical behavior over a wide temperature range

Tong Shen (tdshen@ysu.edu.cn)
Yanshan University https://orcid.org/0000-0002-0391-3361

Kangkang Wen
https://orcid.org/0009-0006-9687-4483

Xuecheng Cai
The University of Hong Kong

B. Sun
Yanshan University

Rui Feng
University of Tennessee at Knoxville

Congcong Du
Yanshan University

Huihui Zhu
University of Science and Technology Beijing

Ke An
Oak Ridge National Laboratory https://orcid.org/0000-0002-6093-429X

Yuan Wu
University of Science and Technology Beijing https://orcid.org/0000-0001-7857-0247

Shuaijun Ding
Yanshan University

Fanxi Meng
Yanshan University

S. Xin
Yanshan University

Zhenhua Bai
Yanshan University

Peter Liaw
University of Tennessee at Knoxville https://orcid.org/0000-0003-0185-3411

Physical Sciences - Article

Keywords:

Posted Date: July 6th, 2023

DOI: https://doi.org/10.21203/rs.3.rs-3126646/v1

Additional Declarations: There is **NO** Competing Interest.

Discovery of a novel low-cost medium-entropy stainless steel with exceptional mechanical behavior over a wide temperature range

Kangkang Wen[1,7], Xuecheng Cai[2,7], Baoru Sun[1,*], Rui Feng[3], Congcong Du[4], Huihui Zhu[5], Ke An[3], Yuan Wu[5], Shuaijun Ding[1], Fanxi Meng[1], Shengwei Xin[1], Zhenhua Bai[1], Peter K. Liaw[6,*], & Tongde Shen[1,*]

[1]Clean Nano Energy Center, State Key Laboratory of Metastable Materials Technology and Science, Yanshan University, Qinhuangdao 066004, China. [2]Department of Mechanical Engineering, The University of Hong Kong, Hong Kong, 999077, China. [3]Neutron Scattering Division, Oak Ridge National Laboratory, Oak Ridge, TN 37831, USA. [4]State Key Laboratory of Physical Chemistry of Solid Surfaces, College of Chemistry and Chemical Engineering, Xiamen University, Xiamen 361005, China. [5]State Key Laboratory for Advanced Metals and Materials, University of Science and Technology Beijing, Beijing 100083, China. [6]Department of Materials Science and Engineering, The University of Tennessee, Knoxville, TN 37996, USA. [7]These authors contributed equally: Kangkang Wen and, Xuecheng Cai. Correspondence and requests for materials should be addressed to B.S. (email: sunbaoru@ysu.edu.cn), P.L. (email: pliaw@utk.edu), or to T.S. (email: tdshen@ysu.edu.cn).

Over 100 years, stainless steels have been extensively used as engineering materials in many areas[1-4]. However, the strength-ductility trade-off[1,3] and insufficient elevated-temperature strength largely hinder their processing and applications. Here, we report a novel Co-free $Fe_{47}Cr_{16}Ni_{26}Ti_6Al_5$ medium-entropy stainless steel (MESS) strengthened by high-density coherent $L1_2$ nanoprecipitates (NPs). We use a thermodynamic approach to pursuing a large volume fraction of stable $L1_2$ NPs in the coarse-grained face-centered-cubic (FCC)-structured matrix of the MESS, which is then readily fabricated through

conventional casting and thermomechanical-treatment techniques. The MESS exhibits a high ultimate tensile strength of 1.35 gigapascals (GPa) and a great total elongation of 36% at room temperature (RT), evading the strength-ductility trade-off dilemma in conventional stainless steels. The high strength is mainly due to the chemical- ordering strengthening of high-density coherent $L1_2$ NPs. The ductile $L1_2$ NPs cooperative with the dynamic refinement of the deformation substructures endow the MESS with an excellent work-hardening ability and a large uniform ductility. Furthermore, the MESS maintains a high yield strength of ~ 0.8 GPa at 700 ^{o}C, which is better than many Fe-based superalloys and stainless steels, even comparable to some Ni-based superalloys. The steady-state creep rates at 750 ^{o}C are at least two orders of magnitude lower than those of conventional Ni-based superalloys and heat-resistant steels. The excellent creep resistance is achieved via the strong interactions between sliding dislocations and stable $L1_2$ NPs at elevated temperatures, which effectively impedes the dislocation movement. The present study has huge potential for designing cost-effective engineering MESSs with excellent mechanical performance for practical applications.

Although renewable energy is on the rise, fossil fuels are likely to remain as the primary source of energy in the coming decades. Thus, it is important to use these resources as efficiently as possible, for both economic reasons and minimization of pollutants[5]. Stainless steels containing Fe, Cr, and Ni elements have been extensively used as high-temperature materials, but they usually exhibit limited strengths at

ambient and elevated temperatures[1,3]. Microstructure refinement is an effective strengthening strategy for stainless steels, whereas it comes at the expense of ductility because of the strength-ductility trade-off. Moreover, fine-grained alloys often suffer from prominent grain growth and considerable reduction in strength (i.e., thermal softening) at high-temperatures[6]. Superalloys comprising high concentrations of Ni, Cr, Co, and Fe elements are used as engineering materials in many fields because they can withstand the high operating temperatures and stresses of components. However, they have a large number of expensive elements, such as Co, Ta, and Mo, resulting in very high production costs[2,4]. On the other hand, some elements (Re and Ru) have been added to superalloys to improve creep strength. Nevertheless, these elemental additions can render alloys to possess higher density and greater cost. Furthermore, the compositions of cast superalloys have to exhibit good castability. However, the addition of heavy elements (Re, W) tends to cause density inversion and results in the formation of casting freckle defects[2,4,7]. Therefore, the development of novel high-performance materials for elevated-temperature applications is urgently needed but is still a great challenge. Unfortunately, the conventional metallurgical-design strategies based on single-principle-element systems, in most cases by adding small amounts of alloying elements or fine-tuning the content of specific elements, have approached their limits for a substantial performance improvement. The emergence of high-entropy alloys (HEAs) and/or medium-entropy alloys (MEAs) presents an unconventional concept and approach[8,9], which have been demonstrated to be one of the most promising structural alloys with a strength-ductility synergy and/or superior

elevated-temperature performance. Nevertheless, these alloys still do not escape from the dilemma of high contents of expensive elements, and it is still challenging to develop cost-effective engineering HEAs/MEAs for wide and practical applications[10-19]. The development of high-performance low-cost Co-free HEAs/MEAs is of great significance and thereby attracts much attention in recent years[20-27].

In this study, we combine a thermodynamics approach that is employed for developing compositionally complex alloys like HEAs/MEAs (see Method) with experimental screening to determine an optimum alloy composition of our Co-free MESS [$Fe_{47}Cr_{16}Ni_{26}Ti_6Al_5$ (atomic percent, at. %)], wherein the contents of Fe, Cr, and Ni are close to those of conventional stainless steels (Fig. 1a) and Fe-based superalloys. The high-resolution neutron-diffraction pattern of the MESS, as shown in the Extended Data Fig. 2a, indicates that the alloy is composed of FCC and $L1_2$ phases. An electron backscatter diffraction (EBSD) image (Fig. 1b) reveals a full recrystallized microstructure, which exhibits a uniform distribution of equiaxed grains with an average size of 70 ± 22 micrometre (μm) (Fig. 1d). Besides, annealing twins are occasionally observed in the matrix (Fig. 1b). The crystallography and chemical composition were further investigated, employing transmission electron microscopy (TEM). The dark-field transmission electron microscopy (DF-TEM) image (Fig. 1c) clearly reveals that a high number density of NPs is uniformly dispersed in the matrix. The average particle size is measured to be ~ 14.4 ± 3.1 nanometer (nm) (Fig. 1d). The selected area electron diffraction (SAED) pattern in the inset of Fig. 1c confirms

112 the $L1_2$-type precipitates, wherein superlattice spots from ordered $L1_2$ NPs,
113 superimposed on the fundamental reflections from the FCC matrix along the [001]
114 direction, are clearly detected. Qualitative energy-dispersive X-ray spectroscopy
115 mapping in the scanning-TEM mode (STEM-EDS) results are presented in the
116 Extended Data Fig. 3a. The FCC matrix phase and the ordered $L1_2$ NPs have
117 distinctively different compositions. Cr is strongly partitioned to the matrix phase
118 forming a solid solution rather than being partitioned to Fe to form a Fe-Cr (σ) phase.
119 Meanwhile, the NPs are revealed to be enriched in Ni and Ti. From the high-angle
120 annular dark-field STEM (HAADF-STEM) (Fig. 1e and Extended Data Figs. 3b and
121 3c), we observe a coherent FCC/$L1_2$ interface with continuous crystal lattices, where
122 the interplanar spacing of the ordered $L1_2$ phase is very close to that of the FCC
123 matrix phase (the lattice mismatch of ~ 0.19%). This trend agrees with the
124 neutron-diffraction results, which suggest that the lattice mismatch between the FCC
125 matrix and the $L1_2$ phase is only ~ 0.124% (Extended Data Fig. 2a). Such a low lattice
126 mismatch would effectively decrease the nucleation barrier, enabling NPs with an
127 extremely high number density (more than 10^{22} m^{-3}) and a small particle size (~ 14.4
128 ± 3.1 nm). Moreover, the HAADF-STEM image (Fig. 1e) confirms that the NP has an
129 $L1_2$-type ordering structure with a sublattice occupied by different elements. The
130 elements with higher atomic numbers (Ni, Fe, and Cr) take up face-centered locations
131 of the FCC crystal lattice, whereas elements with lower atomic numbers (Ti and Al)
132 occupy angular positions (Extended Data Fig. 3c). To further probe the $L1_2$ NPs, we
133 performed three-dimensional atom probe tomography (3D-APT). Atom maps (Fig. 1f)

show that Fe and Cr are enriched in the matrix whereas Ni, Al, and Ti are dominant in the NPs. The three-dimensional morphologies of the ordered $L1_2$ NPs, and the FCC matrix were revealed by reconstructing 60 at. % Ni and 22 at. % Cr iso-concentration surfaces, respectively (Fig. 1f). The stacked NPs can be observed more clearly, wherein the interconnected FCC matrix serves as a frame for the ordered $L1_2$ NPs. The one-dimensional concentration profiles of the phase interface (Fig. 1g) demonstrate that the contents of all alloying elements vary continuously from the FCC matrix to the $L1_2$ NP with a diffuse interface width of ~ 4 nm. The one-dimensional concentration profiles across an individual $L1_2$ NP also exhibit a long-range periodic fluctuation without an abrupt composition change within the NP (Extended Data Fig. 4a). The chemical compositions of the FCC matrix and the $L1_2$ NPs acquired from the flat region of the profiles are $Fe_{55.6}Ni_{16.9}Cr_{20.7}Al_{2.8}Ti_{4.0}$ and $Ni_{66.0}Fe_{7.4}Cr_{1.3}Al_{8.8}Ti_{16.5}$ (at. %), respectively, yielding a (Ni + Fe + Cr): (Al + Ti) ratio of ~ 3:1 (A_3B-type) for $L1_2$ NPs. Using the lever rule analysis[16], the volume fraction of the $L1_2$ phase is determined to be ~ 15% (Extended Data Fig. 4b), which is consistent with the volume fraction of ~17.3% determined by the Rietveld refinement from neutron-diffraction patterns (Extended Data Fig. 2a).

Figure 2a and Extended Data Fig. 5 exhibit the tensile stress-strain curves of the MESS performed from room temperature (RT) to 800 °C. A base alloy ($Fe_{47}Cr_{16}Ni_{26}$, see Methods) was also tested for comparison. The MESS exhibits an extraordinary combination of high strength and great ductility. The RT yield strength (σ_y) and ultimate tensile strength (σ_u) of MESS are as high as 927 and 1,353 megapascals

(MPa), respectively. Note that the σ_y of MESS is five times that (165 MPa) of the base alloy (Fig. 2a). Surprisingly, such a high strength comes with a high uniform elongation of 30% and a great total elongation (ε) of 36%. At such a high σ_y, the MESS still shows a strong strain-hardening ability ($\sigma_u - \sigma_y > 400$ MPa, $\sigma_y/\sigma_u < 0.7$). According to the Considere's criterion, homogeneous deformation can be maintained when the strain-hardening rate (SHR), $d\sigma/d\varepsilon$, is above the flow stress, σ[28]. Thus, the higher the SHR, the greater the ductility. The higher SHR of the FeCrNiTiAl MESS - when compared with the FeCrNi base alloy - (Fig. 2b) endows it with a satisfactory homogeneous ductility (Fig. 2a). Moreover, the MESS presents a typical three-stage feature of strain hardening, which has been commonly observed in precipitation-strengthened alloys. The corresponding strain-distribution maps obtained by digital image correlations (DIC) at various global strains and at ambient temperature are exhibited in Fig. 2c. The sample shows a very diffuse strain distribution throughout the gauge section when being strained below 30% [Figs. 2(c1) - (c3)], indicating a homogenous deformation. As the deformation proceeds, necking occurs at a ~ 30% strain [a red dashed frame in Fig. 2(c4)], and the sample quickly fractures due to a significant strain localization [Fig. 2(c5)]. The MESS also exhibits superior elevated-temperature mechanical performances. Not much drop in both the yield strength and ductility but an obvious serrated response is observed between 300 and 500 °C (Extended Data Fig. 5). The σ_y values of the MESS at 600 °C and 700 °C are still as high as 808 MPa and 802 MPa, respectively (Fig. 2a and Extended Data Fig. 5). Noteworthy, the MESS maintains a high strain-hardening rate at 600 °C (Fig.

178 2b), resulting in a high σ_u of 1,074 MPa (Fig. 2d and Extended Data Fig. 5). The
179 dimple morphology of the fracture surface confirms the intrinsic ductile feature of the
180 MESS at room and elevated temperatures (Extended Data Fig. 6). The fractographic
181 feature changes from a transgranular fracture mode (below 600 ^{o}C, Extended Data Fig.
182 6a) to a mixed mode of intergranular and transgranular fracture (600 ^{o}C, Extended
183 Data Fig. 6b) and then to intergranular fracture (700 ^{o}C, Extended Data Fig. 6c).
184 To reveal the underlying mechanisms for the three-stage hardening behavior, the
185 evolution of the microstructures of the MESS deformed to different strains (3%, 10%,
186 23%, and fracture) were examined. The sharp decline of the SHR (Fig. 2b) of MESS
187 at the early strain stage (< 3% strain, stage 1) after yielding can be attributed to the
188 prevalence of dislocations re-arrangement, such as the cross-slip and annihilation of
189 screw dislocations of opposite signs[24,28]. At a strain of ~ 3% (Fig. 3a), dislocation slip
190 is preferentially activated at the grain boundary, and planar-arrayed slip bands lying
191 essentially on {111} planes of the matrix appear. With further straining, the SHR
192 drops slowly (Fig. 2b). It can be clearly observed that the dislocations operated
193 mainly in a planar way, wherein dense {111} plane slip bands are characterized at a
194 strain of 10% of the MESS (Fig. 3b). The deformation mode transits from a cross slip
195 to planar slip, indicating that the underlying deformation starts to be dominated by the
196 enhanced ordering effect[29]. Meanwhile, more dislocations are further activated in
197 grain interiors (Fig. 3b). Figure 3c indicates that the coherent NPs have been fully
198 sheared by these cutting dislocations. The inverse fast Fourier transformation (IFFT)
199 pattern (Fig. 3c inset image) taken near the dislocation cutting point (the upper left

200 black circles of Fig. 3c) reveals a profuse multiplication of edge dislocations,
201 indicative of a remarkable strain-hardening capability of the material. With increasing
202 the strain to 23%, the dislocations continue operating in a planar way, forming a
203 substructure of Taylor lattices (yellow arrows), where the dislocation motion is
204 confined to the {111} primary slip systems (Fig. 3d). The averaged interspacing of
205 these deformation substructures decreases from about 1 μm (slip bands at a 10%
206 strain) to less than 200 nm (Taylor lattice at a 23% strain) as the plastic strain
207 progresses. Such a pronounced planar slip of dislocations can be attributed to the
208 existence of high-density coherent $L1_2$ ordered NPs, since it has been demonstrated
209 that the shearable precipitates as well as the short-range order can significantly
210 promote slip planarity[30]. A similar observation has also been identified in a
211 Fe-Mn-Al-C steel with nano-sized carbides[31]. The continuous multiplication and
212 intersection of the planar slip bands result in a dynamic subdivision and refinement of
213 matrix grains during deformation. The refinement and intersection of these
214 deformation substructures can serve as an effective carrier for dislocation
215 accumulation, giving rise to an enhanced strain hardening, and being helpful to delay
216 the onset of plastic instability[28,32,33]. Thus, the slip bands refinement is the dominant
217 mechanism for the high SHR (Fig. 2b) and high ductility of MESS, namely the
218 slip-bands-refinement-induced plasticity (SRIP) effect[13,33]. Figures 3d and f shows the
219 deformation substructures of the fractured sample. To accommodate the large
220 macro-strain, the accumulated in-plane dislocations of the Taylor lattice further
221 transform into crystallographically aligned high-density dislocation walls (HDDWs)

222 and microbands (MBs). The diffraction vector shows that they are near parallel to the
223 trace of the {111} slip plane, demonstrating that they are the substructures induced by
224 a further refinement of slip bands[13,33], which dominate the late-stage deformation
225 process (nonuniform deformation) until the fracture failure occurs[13]. Note that the
226 fully coherent relationship among the FCC matrix, $L1_2$ NPs, and the nanometer-scale
227 particle size of these NPs can also contribute to the ductility of the MESS. Hence, the
228 external force can be uniformly dispersed at coherent interfaces between the
229 precipitates and matrix[34], and the stress concentration can be largely alleviated,
230 effectively inhibiting the premature nucleation of cracks.
231 The strengthening and ductile nature of the $L1_2$ NPs are well evidenced by in-situ
232 neutron-diffraction results (Fig. 4). The behavior of lattice strain under a true stress at
233 both RT and 600 ^{o}C (Figs. 4a and 4b) indicates that the $L1_2$ NPs can not only
234 strengthen the matrix but also co-deform with it, as evidenced by the greatly increased
235 lattice strains of $L1_2$'s unique {210} and {211} diffraction peaks after yielding, i.e.,
236 the increasing rate of lattice strains, compared to those fundamental $L1_2$/FCC
237 diffraction peaks. Notably, the $L1_2$'s unique {210} and {211} diffraction peaks deflect
238 together with the fundamental diffraction peak of {220} (indicated by the red arrow),
239 suggesting a co-deformation behavior between the $L1_2$ NPs and the FCC matrix. In
240 addition, the plastic deformability of the precipitates can be assessed by examining
241 the ratio of the full width at half-maximum (FWHM) to the d-spacing[35]. In this case,
242 the greatly increased FWHM/d values of the {210} and {211} diffraction peaks of $L1_2$
243 NPs as a function of true strain (Figs. 4c and 4d) clearly demonstrate their ability to

undergo plastic deformation. Consequently, the high-density coherent and ductile $L1_2$ NPs working together with the dynamic refinement of the deformation substructures during plastic deformation endow the MESS with an excellent strain-hardening ability and a large uniform ductility.

The precipitation strengthening from high-density $L1_2$ NPs together with solid-solution strengthening and dislocation hardening elevate the yield strength of the MESS to near 1 GPa (see Methods), wherein the precipitation-strengthening offers the greatest contribution (~ 60%) to the yield strength. Moreover, the precipitation-strengthening effect remains active at elevated temperatures, which can be evidenced by the plot of the lattice strain versus true stress at 600 ^{o}C (Fig. 4b). It is observed that the lattice strains of $L1_2$'s unique {210} and {211} diffraction peaks continue to increase beyond ~ 900 MPa, while the lattice strains of the fundamental diffraction peaks of FCC/ $L1_2$, e.g., {111} and {200}, begin to deflect towards smaller values. This behavior indicates that even at 600 °C, the $L1_2$ NPs continue to bear a larger load and serve as a source of strengthening. Extended Data Fig. 7 shows the deformation microstructure of the 10%-strained sample at 600 ^{o}C. Planar dislocation slips on the {111} planes are prevalent (Extended Data Fig. 7a), exhibiting a similar deformation mechanism to that at RT (Fig. 3b). The close-up view (Extended Data Fig. 7b) further reveals that the coherent $L1_2$ NPs within the planar slip bands are intensively sheared by the planar dislocations. The ordering strengthening from the densely coherent $L1_2$ NPs is supposed to remain effective at elevated temperatures, endowing the MESS with a good combination of high yield strength and reasonable

work-hardening ability at elevated temperatures up to 600 °C (Fig. 2b). In addition, previous work has indicated that $L1_2$ NPs can remain stable after aging at the elevated temperatures (between 525 and 600 °C)[36]. Particularly, the $L1_2$ NPs of our MESS grew gradually from 14.4 ± 3.1 nm to 27.7 ± 5.2 nm and maintained a spherical morphology after a high-temperature treatment at 700 °C for 200 hours (h) (Extended Data Figs. 8a and b). The superior thermal and structure stability can be mainly ascribed to the coherent FCC/$L1_2$ interface[37], which sustains a small lattice mismatch (0.42%) at 700 °C (Extended Data Fig. 8c). However, the ductility remarkably decreases at 700 °C. Such a degradation of ductility is generally attributed to the precipitation of the brittle $L2_1$ phase at grain boundaries (Extended Data Fig. 9), which can account mainly for the transition from the intragranular to intergranular fracture (Extended Data Fig. 6). Nevertheless, the $L2_1$ phase was not well captured by the neutron-diffraction measurements at both RT and 600 °C. Instead, only a very minor $L2_1$'s 220 peak was observed (Extended Data Figs. 2a and 2b), indicating a very low content, which may not seriously deteriorate the ductility of the MESS at temperatures below 700 °C. Similar embrittling behaviors have also been frequently observed in many commercial Ni-based superalloys, such as the U720Li, Waspaloy, GH4033, etc.[2,38].

Figure 5a shows a comparison of RT-mechanical properties of the MESS with those of commercial stainless steels, Fe-based superalloys, and Co-free Fe-, and Ni-based HEAs/MEAs. The present MESS exhibits yield strength two to four times that of austenitic-stainless steels and a higher product of σ_u and ε [3]. Besides, the product of

σ_u and ε of our MESS (~ 50 GPa · %) is four to five times those of precipitation-hardening (PH) stainless steels with comparable strengths[3]. Moreover, compared to the body-centered-cubic (BCC)-structured stainless steels [ferritic (F), martensitic (M), and M-F duplex], our MESS displays a two to three times yield strength and product of σ_u and ε[3]. Even when compared with the Fe-based superalloys[2] and recently reported Co-free Fe- and Ni-based HEAs/MEAs[20-27], our MESS also displays a higher strength-ductility combination. The exceptional combination of the high strength and large ductility distinguishes our MESS from other commercial stainless steels, Fe-based superalloys, and most Co-free Fe-, and Ni-based HEAs/MEAs. We also compare the elevated-temperature strength of our MESS with some conventional Fe-based superalloys and Co-free HEAs/MEAs (Fig. 5b)[2,22,39-41]. Almost no decay in the high yield strength (~ 800 MPa) of the MESS can be observed at temperatures below 700 °C. This high yield strength well exceeds those of most Fe-based superalloys and Co-free HEAs/MEAs. Even at a high temperature of 800 °C, our MESS still has a relatively high yield strength of ~ 600 MPa. The creep resistance of our MESS was also evaluated.

High creep resistance is required for materials used at high temperatures. Conventional ferritic and austenitic heat-resistant stainless steels, however, do not have sufficient creep resistance in harsh environments[1]. The γ prime phase-precipitation strengthened Ni-based superalloys exhibit good creep strength and corrosion resistance at high temperatures of 700 °C and above. Nevertheless, these Ni-based superalloys are excessively expensive due to the high content of Co (10 - 20

weight percent, wt. %) and/or Mo and W (6 - 8 wt. %)[2]. We performed tensile creep tests of our low-cost MESS at a high temperature of 750 °C. Figure 5c shows the creep strain versus time curves at different applied stresses. The creep strain is observed to increase with the applied stress, whereas the MESS crept at 100 MPa shows a small creep strain of less than 4% after 300 h. This is a very demanding creep-test condition, where conventional alloys, such as a type 347 stainless steel ruptured within ~ 100 to 300 h[42]. We further calculated the steady-state creep rate at different applied stresses, as displayed in Fig. 5d. At the higher stress level (750 °C/300 MPa), the steady-state creep rate of the MESS is 4.89×10^{-7} s^{-1}, which is at least 3 orders of magnitude lower than those of conventional Ni-based superalloys, such as Haynes 282[43] (6.4×10^{-4} s^{-1} at 760 °C/290 MPa), Inconel 740[44] (4.1×10^{-4} s^{-1} at 750 °C/300 MPa), and Sanicro 25[45] (1.46×10^{-3} s^{-1} at 750 °C/240 MPa).

The deformation-microstructure analysis was performed in creep-strained specimens in order to explore the interactions between dislocations and $L1_2$ NPs. The bright-field (BF) TEM image (Extend Data Fig. 10a) shows dislocation configurations of the alloy crept at 750 °C/70 MPa for 300 h. Most of the dislocations are observed to be strongly curved, revealing an effective impediment of NPs on dislocation movement. The inset of Extend Data Fig. 10a presents the interaction details, where dislocation climbing up the $L1_2$ NPs can be clearly identified. The dislocation climbing is principally accommodated by the long-range diffusion of vacancies, retarding dislocations to overcome obstacles. A low steady-state creep rate (~ 1.71×10^{-8} s^{-1}) is thus obtained during creep deformation under a relatively small, applied stress of 70 MPa.

Meanwhile, some discrete dislocation loops can also be observed, as indicated by the yellow arrows in Extend Data Fig. 10a, indicating that the Orowan bypassing process is activated. The size-dependent critical resolved shear stress (CRSS) for Orowan looping can be estimated as[46]: $\tau_c = Gb/l$ where τ_c is the CRSS, G is the shear modulus, b is the Burgers vector, and l is the inter-particle spacing. Assuming that the volume fraction of the particle remains constant, the average inter-particle spacing, l, increases with precipitates coarsening. It is noted that particle ripening would inevitably occur to some extent in the later stage of the high-temperature creep, leading to a decrease of the Orowan shear stress and dislocation looping around the coarser precipitates. The BF-TEM image (Extend Data Fig. 10b) shows dislocation configurations of the alloy crept at 750 ^{o}C/150 MPa for 128 h, where prevalent dislocation shearing through $L1_2$ NPs can be clearly observed. It can be inferred that the increased applied stress (150 MPa) enables dislocations to overcome the shear resistance of $L1_2$ NPs, resulting in a slip-plastic deformation. The dislocation shearing is identified as the dominant deformation mechanism during the creep process at 750 ^{o}C/150 MPa under the present circumstances. In either case, the interactions between dislocations and $L1_2$ NPs can impede the movement of dislocations, thus effectively enhancing the creep resistance of MESS.

Extended Data Fig. 11a shows the comparison between the ultimate tensile strength (UTS) and the raw material costs for typical 304 austenitic-stainless steels, Fe-based superalloys[2,4], some recently reported HEAs/MEAs[13,18,24,47-50], and the present MESS. As can be seen, our MESS not only produces impressive mechanical properties, but

also has a raw material cost lower than most of the counterparts. Moreover, we have also used the parameter of the ratio of UTS to the raw material costs to further manifest the strengthening efficiency of a promising material. As can be seen from the Extended Data Fig. 11b, our MESS shows a great advantage in potential engineering applications.

In conclusion, we have developed a novel MESS with an excellent strength-ductility synergy over a wide temperature range, which can be fabricated readily through conventional casting and thermomechanical treatment techniques. Our material design principle has huge potential for fabricating cost-effective engineering MESS with exceptional mechanical performance to replace, at least partially, both conventional low-strength stainless steels and expensive nickel-based superalloys that are widely utilized worldwide.

1. Lo, K. H., Shek, C. H. & Lai, J. K. L. Recent developments in stainless steels. *Mater. Sci. Eng. R.* **65**, 39-104 (2009).
2. Geddes, B., Leon, H. & Huang, X. *Superalloys: alloying and performance*. (Asm International, 2010).
3. Outokumpu Stainless, A. *Handbook of stainless steel*. (Nova Science 2013).
4. Yvon, P. *Structural materials for generation IV nuclear reactors*. (Woodhead publishing, 2016).
5. Welsby, D., Price, J., Pye, S. & Ekins, P. Unextractable fossil fuels in a 1.5 degrees C world. *Nature* **597**, 230-234 (2021).

6. Olander, D. R. Structural Materials in Nuclear Power Systems. *Nucl. Sci. Eng.* **80**, 204-205 (1982).

7. Pollock, T. M. Alloy design for aircraft engines. *Nat. Mater.* **15**, 809-815 (2016).

8. Cantor, B., Chang, I. T. H., Knight, P. & Vincent, A. J. B. Microstructural development in equiatomic multicomponent alloys. *Mater. Sci. Eng. A* **375-377**, 213-218 (2004).

9. Yeh, J. W. *et al.* Nanostructured high-entropy alloys with multiple principal elements: Novel alloy design concepts and outcomes. *Adv. Eng. Mater.* **6**, 299-303 (2004).

10. Gludovatz, B. *et al.* A fracture-resistant high-entropy alloy for cryogenic applications. *Science* **345**, 1153-1158 (2014).

11. Zhang, Y. *et al.* Microstructures and properties of high-entropy alloys. *Prog. Mater. Sci.* **61**, 1-93 (2014).

12. Li, Z., Pradeep, K. G., Deng, Y., Raabe, D. & Tasan, C. C. Metastable high-entropy dual-phase alloys overcome the strength-ductility trade-off. *Nature* **534**, 227-230 (2016).

13. Yang, T. *et al.* Multicomponent intermetallic nanoparticles and superb mechanical behaviors of complex alloys. *Science* **362**, 933-937 (2018).

14. George, E. P., Raabe, D. & Ritchie, R. O. High-entropy alloys. *Nat. Rev. Mater.* **4**, 515-534 (2019).

15. Du, X. H. *et al.* Dual heterogeneous structures lead to ultrahigh strength and uniform ductility in a Co-Cr-Ni medium-entropy alloy. *Nat. Commun.* **11**, 2390 (2020).

16. Fan, L. *et al.* Ultrahigh strength and ductility in newly developed materials with coherent nanolamellar architectures. *Nat. Commun.* **11**, 6240 (2020).

17. Pan, Q. *et al.* Gradient cell-structured high-entropy alloy with exceptional strength and

ductility. *Science* **374**, 984-989 (2021).

18. Shi, P. *et al.* Hierarchical crack buffering triples ductility in eutectic herringbone high-entropy alloys. *Science* **373**, 912-918 (2021).

19. Liu, D. *et al.* Exceptional fracture toughness of CrCoNi-based medium-and high-entropy alloys at 20 kelvin. *Science* **378**, 978-983 (2022).

20. Meng, F., Qiu, J. & Baker, I. The effects of chromium on the microstructure and tensile behavior of $Fe_{30}Ni_{20}Mn_{35}Al_{15}$. *Mater. Sci. Eng. A* **586**, 45-52 (2013).

21. Ng, C. *et al.* Phase stability and tensile properties of Co-free $Al_{0.5}CrCuFeNi_2$ high-entropy alloys. *J. Alloy. Compd.* **584**, 530-537 (2014).

22. Shaysultanov, D. G. *et al.* Novel $Fe_{36}Mn_{21}Cr_{18}Ni_{15}Al_{10}$ high entropy alloy with bcc/B2 dual-phase structure. *J. Alloy. Compd.* **705**, 756-763 (2017).

23. Wang, Z., Genc, A. & Baker, I. Direct versus indirect particle strengthening in a strong, ductile FeNiMnAlTi high entropy alloy. *Mater. Charact.* **132**, 156-161 (2017).

24. Zhao, Y. L. *et al.* Development of high-strength Co-free high-entropy alloys hardened by nanosized precipitates. *Scr. Mater.* **148**, 51-55 (2018).

25. Ji, Y. *et al.* Microstructure and tensile properties of Co-free $Fe_4CrNi(AlTi)$ high-entropy alloys. *Intermetallics* **138** (2021).

26. Yang, Y. *et al.* Bifunctional nanoprecipitates strengthen and ductilize a medium-entropy alloy. *Nature* **595**, 245-249 (2021).

27. Fan, J. *et al.* Unveiling the precipitation behavior and mechanical properties of Co-free $Ni_{47-x}Fe_{30}Cr_{12}Mn_8Al_xTi_3$ high-entropy alloys. *J. Mater. Sci. Technol.* **118**, 25-34 (2022).

28. Courtney, T. H. *Mechanical behavior of materials*. (Waveland Press, 2005).

29. Jiang, S. *et al.* Ultrastrong steel via minimal lattice misfit and high-density nanoprecipitation. *Nature* **544**, 460-464 (2017).

30. Gerold, V. & Karnthaler, H. P. On the origin of planar slip in f.c.c. alloys. *Acta. Metall.* **37**, 2177-2183 (1989).

31. Gutierrez-Urrutia, I. & Raabe, D. Multistage strain hardening through dislocation substructure and twinning in a high strength and ductile weight-reduced Fe-Mn-Al-C steel. *Acta. Mater.* **60**, 5791-5802 (2012).

32. Yoo, J. D. & Park, K.-T. Microband-induced plasticity in a high Mn-Al-C light steel. *Mater. Sci. Eng. A* **496**, 417-424 (2008).

33. Haase, C. *et al.* On the deformation behavior of κ-carbide-free and κ-carbide-containing high-Mn light-weight steel. *Acta. Mater.* **122**, 332-343 (2017).

34. Gao, J. *et al.* Facile route to bulk ultrafine-grain steels for high strength and ductility. *Nature* **590**, 262-267 (2021).

35. Feng, R. *et al.* Enhancing fatigue life by ductile-transformable multicomponent B2 precipitates in a high-entropy alloy. *Nat. Commun.* **12**, 3588 (2021).

36. Vittori, M. & Mignone, A. On the antiphase boundary energy of Ni_3(Al, Ti) particles. *Mater. Sci. Eng.* **74**, 29-37 (1985).

37. Lu, W., Luo, X., Huang, B., Li, P. & Yang, Y. Excellent thermal stability and their origins in γ' precipitation-strengthened medium-entropy alloys. *Scr. Mater.* **212** (2022).

38. Németh, A. A. N. *et al.* Environmentally-assisted grain boundary attack as a mechanism of embrittlement in a nickel-based superalloy. *Acta. Mater.* **126**, 361-371 (2017).

39. Kuznetsov, A. V., Shaysultanov, D. G., Stepanov, N. D., Salishchev, G. A. & Senkov, O. N.

442 Tensile properties of an AlCrCuNiFeCo high-entropy alloy in as-cast and wrought conditions.
443 *Mater. Sci. Eng. A* **533**, 107-118 (2012).
444 40. Daoud, H. M., Manzoni, A. M., Wanderka, N. & Glatzel, U. High-Temperature Tensile
445 Strength of $Al_{10}Co_{25}Cr_8Fe_{15}Ni_{36}Ti_6$ Compositionally Complex Alloy (High-Entropy Alloy).
446 *JOM* **67**, 2271-2277 (2015).
447 41. Jiang, W., Yuan, S., Cao, Y., Zhang, Y. & Zhao, Y. Mechanical properties and deformation
448 mechanisms of a $Ni_2Co_1Fe_1V_{0.5}Mo_{0.2}$ medium-entropy alloy at elevated temperatures. *Acta.*
449 *Mater.* **213** (2021).
450 42. Yamamoto, Y. *et al.* Creep-resistant, Al_2O_3-forming austenitic stainless steels. *Science* **316**,
451 433-436 (2007).
452 43. Wang, L. *et al.* Effect of heterogeneous microstructure on the tensile and creep performances
453 of cast Haynes 282 alloy. *Mater. Sci. Eng. A* **828** (2021).
454 44. Evans, N. D., Maziasz, P. J., Swindeman, R. W. & Smith, G. D. Microstructure and phase
455 stability in INCONEL alloy 740 during creep. *Scripta Materialia* **51**, 503-507 (2004).
456 45. Zhang, Y. *et al.* High-temperature deformation and fracture mechanisms of an advanced heat
457 resistant Fe-Cr-Ni alloy. *Mater. Sci. Eng. A* **686**, 102-112 (2017).
458 46. Sun, F., Gu, Y. F., Yan, J. B., Zhong, Z. H. & Yuyama, M. Phenomenological and
459 microstructural analysis of intermediate temperatures creep in a Ni–Fe-based alloy for
460 advanced ultra-supercritical fossil power plants. *Acta. Mater.* **102**, 70-78 (2016).
461 47. He, J. Y. *et al.* A precipitation-hardened high-entropy alloy with outstanding tensile properties.
462 *Acta. Mater.* **102**, 187-196 (2016).
463 48. Liang, Y. J. *et al.* High-content ductile coherent nanoprecipitates achieve ultrastrong

high-entropy alloys. *Nat. Commun.* **9**, 4063 (2018).

49. Shi, P. *et al.* Enhanced strength-ductility synergy in ultrafine-grained eutectic high-entropy alloys by inheriting microstructural lamellae. *Nat. Commun.* **10**, 489 (2019).

50. Lu, W. et al. Superb strength and ductility balance of a Co-free medium-entropy alloy with dual heterogeneous structures. *J. Mater. Sci. Technol.* **98**, 197-204 (2022).

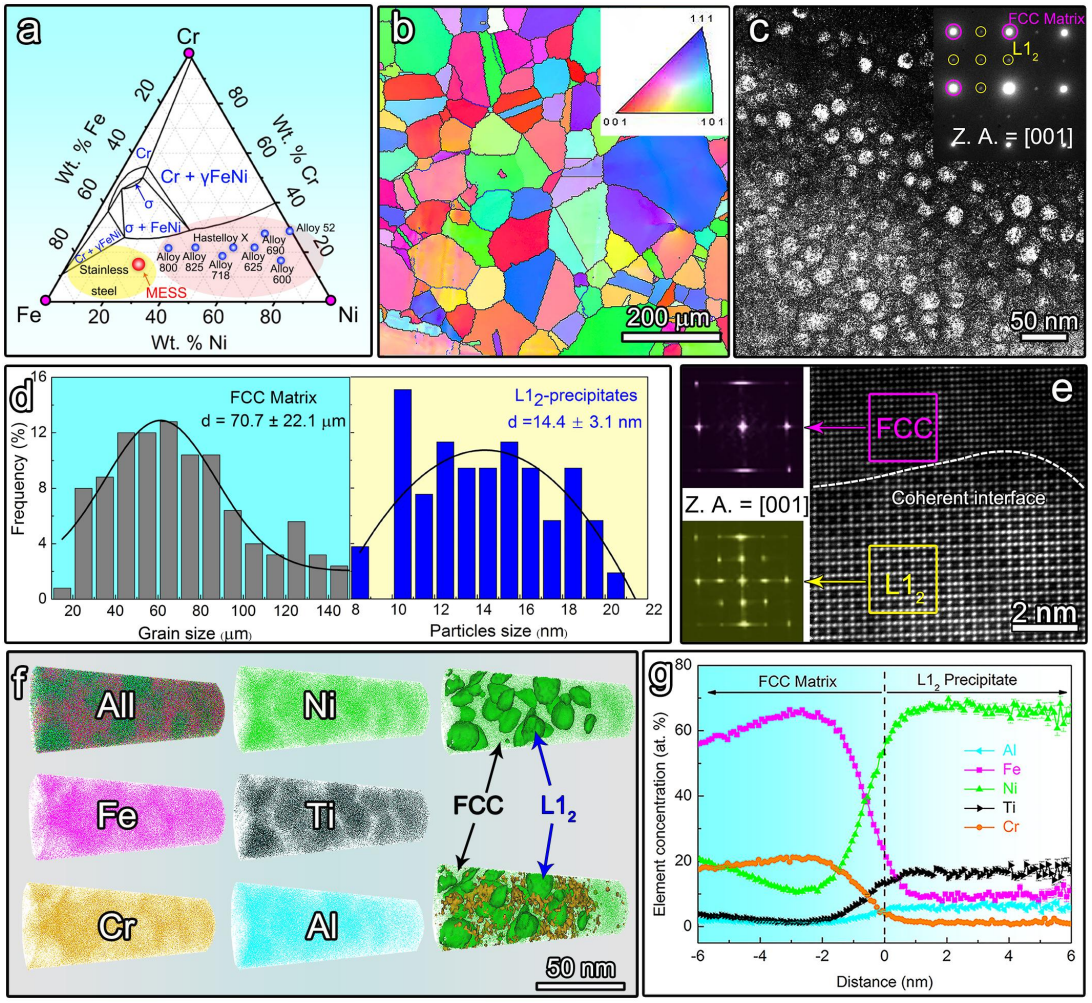

Fig. 1 | Conceptual design and microstructural characterizations of the MESS. a Position of our alloy in the Fe-Cr-Ni phase diagram falling within the composition range of stainless steels. **b** EBSD image of the MESS with equiaxed grains. **c** DF-TEM image of the MESS showing the high-density NPs. The SAED pattern in the inset verifying the $L1_2$-type of the NPs. **d** Statistical distributions for the average size of the FCC matrix grains and $L1_2$ NPs (d denotes the average size). **e** High-resolution STEM image illustrating the interfacial coherency of the FCC matrix/$L1_2$ NP (Z. A. denotes the zone axis). **f** Representative atom maps collected from the MESS, using the 3D-APT showing the distribution of each element. Fe and Cr are enriched in the matrix, whereas Ni, Al, and Ti are enriched in the NPs, and three-dimensional reconstruction of 60 at. % Ni and 22 at. % Cr iso-concentration surfaces presenting the morphologies of the ordered $L1_2$ NPs and the FCC matrix. **g** One-dimensional concentration profiles showing the elemental distributions from the matrix to the NP.

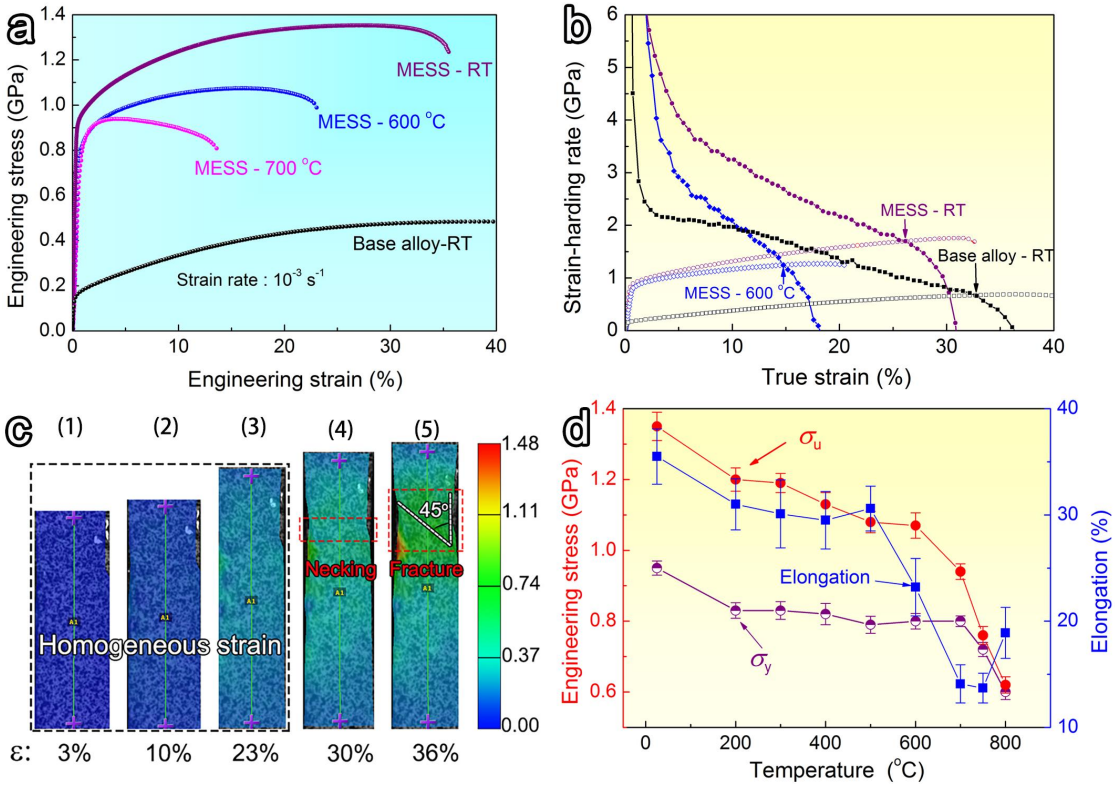

484 **Fig. 2 | Exceptional strength-ductility combination of the MESS. a** Uniaxial
485 engineering tensile stress-strain curves at different temperatures. **b** Strain-hardening rate
486 versus true strain. The intersections with the true stress–strain curves are marked with
487 arrows to indicate the onset of necking instability. **C** Strain-field distribution of the MESS
488 during tensile testing at ambient temperature (field of view: 5.2 mm × 2.2 mm). Evolution
489 of micro-strains along the loading direction at different macro-strains: 3% (**c**1), 10% (**c**2),
490 23% (**c**3), 30% (**c**4), and 36% (**c**5). **D** Variations of σ_y, σ_u, and elongation of the MESS
491 with testing temperature.
492

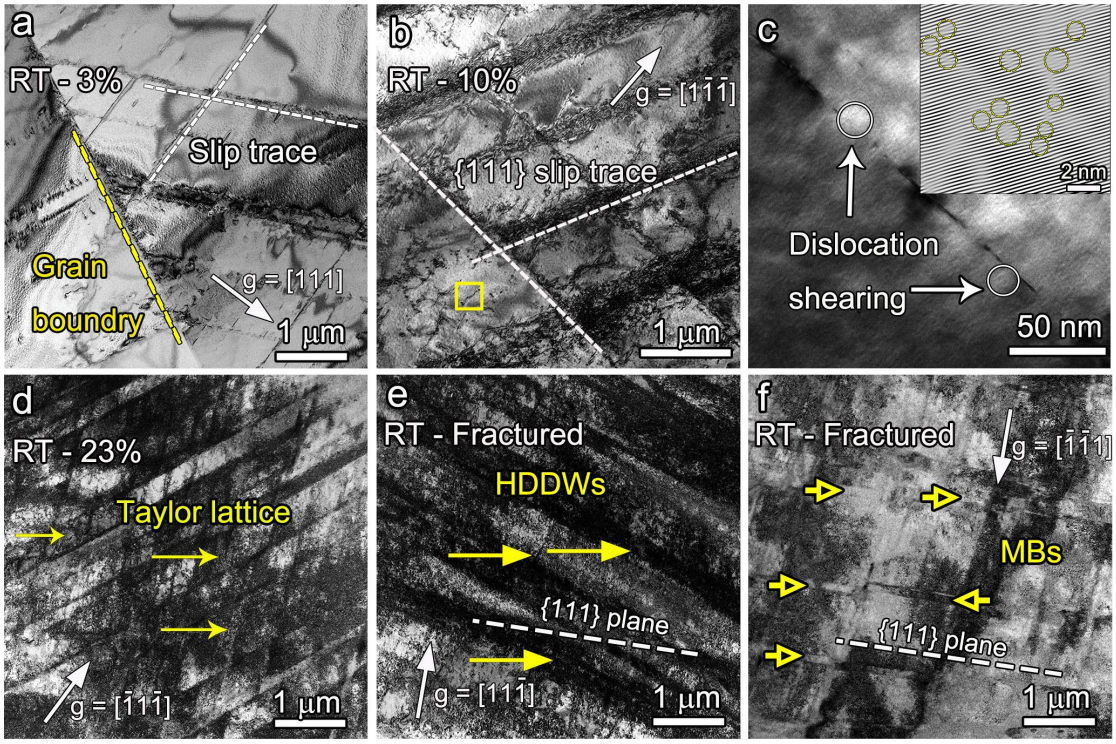

493 **Fig. 3** | **Deformation microstructures of the MESS at RT. a** Deformation microstructure
494 of the 3%-strained sample. Grain boundary (yellow arrow) emits dislocations, and a small
495 amount of slip trace (white dashed line) occurs in the form of the planar dislocation slip. **b**
496 Activations of more {111} slip traces (white dashed line) at the 10% strain. **c** A close-up
497 view of the region marked by the yellow rectangle in **b** revealing that dislocations shear
498 through $L1_2$ NPs. The IFFT image in the inset showing the profuse multiplication of edge
499 dislocations (in yellow dashed circles) near the dislocation cutting point (inside the upper
500 left white circle). **d** High-density {111} slip traces leading to the formation of Taylor lattices
501 (yellow arrow) at the 23% strain. **e. f** Deformation microstructures of the fractured MESS.
502 At high strains, HDDWs (**e**) and MBs (**f**) were formed. The slip trace shows that the MBs
503 are parallel to the trace of the {111} glide plane (white dashed line).
504

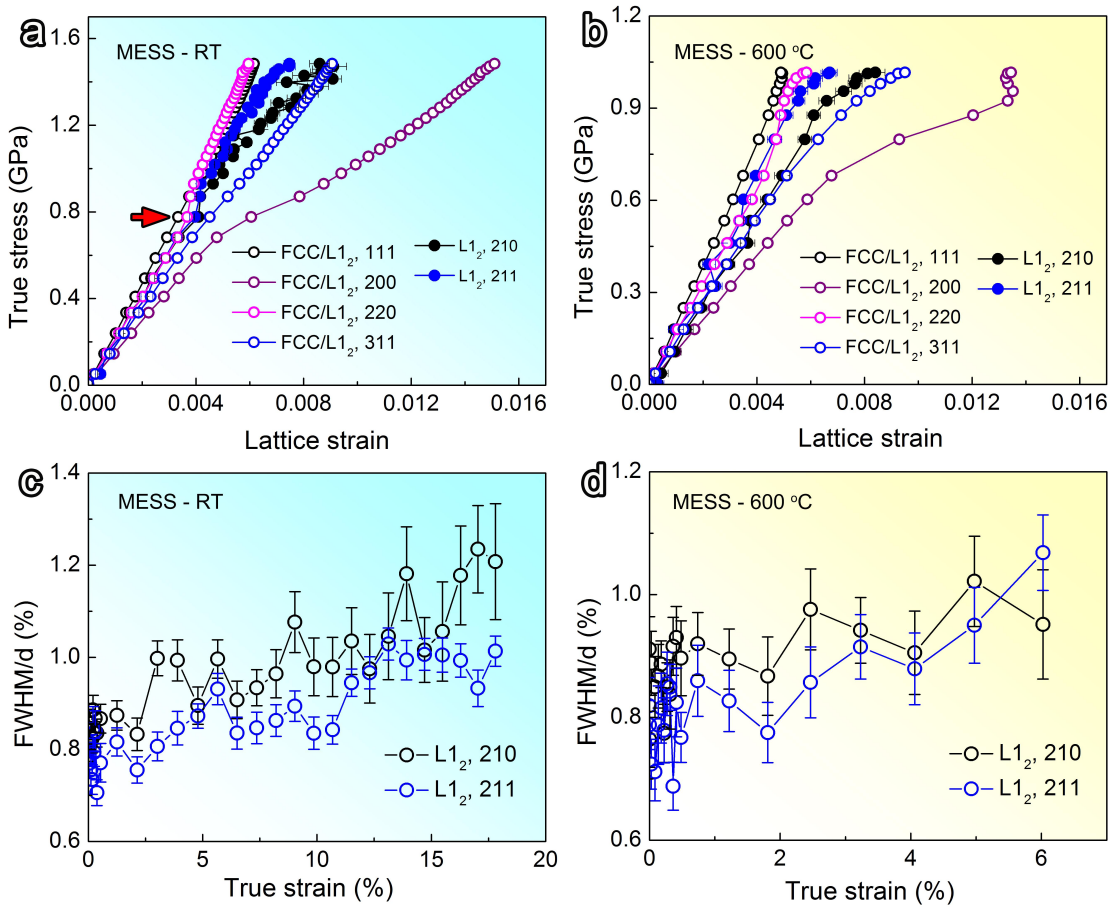

505 **Fig. 4 | In-situ neutron-diffraction results. a** and **b** Lattice strain as a function of true
506 stress during tensile deformation at RT and 600 °C, respectively, showing the load transfer
507 from the soft matrix to the hard $L1_2$ NPs, a reflection of the precipitation strengthening. **c**
508 and **d** Evolution of FWHM/d as a function of true strain, indicating the ductile nature of the
509 multicomponent $L1_2$ NPs.
510

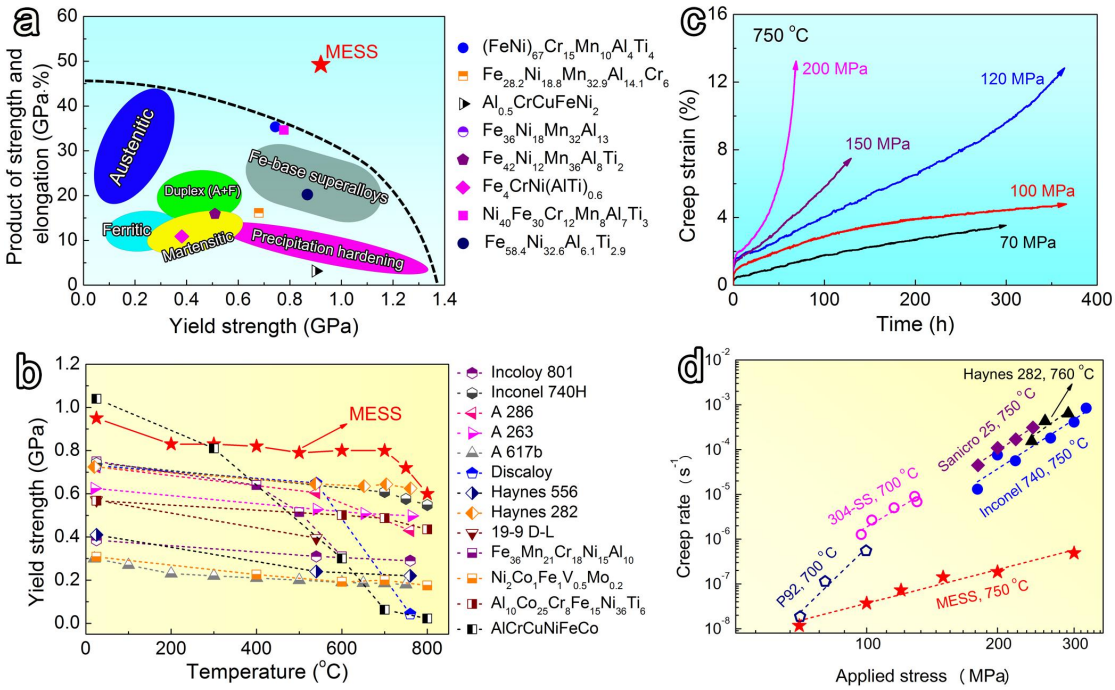

511 **Fig. 5 | Mechanical properties of our MESS compared with other alloys. a** Yield
512 strength versus the product of the ultimate tensile strength and ductility of the MESS,
513 compared with those of stainless steels, Fe-based superalloys, and some Co-free
514 HEAs/MEAs. **b** Variation of yield strength with testing temperature of the MESS,
515 compared with those of conventional stainless steels, Fe-based superalloys, and some
516 HEAs/MEAs. There, of course, are a few advanced Ni-based superalloys and stainless
517 steels not shown for comparison, due to their difficulty to achieve mass industrial
518 production (for example, additive manufacturing, high-pressure torsion, and
519 liquid-nitrogen cold rolling). Some high Co and, Ni content (more than 50 at. %)
520 HEAs/MEAs are not shown for comparison because of expensive costs, as well. **c** Creep
521 strain versus time curves of the MESS at 750 ºC under different applied stresses, the
522 arrows denote the that samples are not fractured during creep testing. **d** Creep rate
523 versus applied stress curves of the MESS and some other conventional Ni-based
524 superalloys and heat-resistant steels.
525

Methods

Compositional design and phase calculation. The ternary FeCrNi alloy with an FCC structure was initially chosen as the base alloy, which was then alloyed with Ti and Al to generate $L1_2$-type coherent NPs. Three main criteria were considered in the alloy-design process. First, a high content of Cr (~ 16 at. %) - close to that of the 304 stainless steel - is selected in the base alloy. The high content of Cr can promote the phase separation[51] and reduce the difference in the lattice parameters between the FCC matrix and $L1_2$ NPs[52], thereby stabilizing the coherent interfaces[53] and lowering the driving force for competitive coarsening[29]. Additionally, a high content of Cr can also render the MESS a superior corrosion and oxidation resistance[1]. Second, a high content of Ni is expected, which can facilitate the precipitation of $L1_2$ NPs as much as possible. However, the Ni content should be kept as low as possible to promote the wide applicability of our MESS. The Ni content in our MESS is thus ideally controlled within 28 at. % - which is the maximum amount of Ni in stainless steels - to ensure a comparable material cost to commercial stainless steels. Third, $L1_2$ NPs should remain as stable as possible at high temperatures, while inhibiting the formation of other brittle intermetallic compounds in MESS. Under the circumstances, the addition of Al and Ti should be well controlled to ensure a stabilized matrix phase without excess complex phases.

The empirical criteria, $\Omega = T_m\Delta S_{mix}/\Delta H_{mix} \geq 1.1$ and $\delta \leq 6.6\%$, - which have been widely used to predict a stable solid-solution matrix in HEAs - are utilized to optimize the contents of Al and Ti in our MESS. Meanwhile, Ω should approach the threshold

548 value of 1.1, where the formed secondary phases may be more beneficial for
549 mechanical performance (i.e., coherent precipitates). Herein the parameters, ΔH_{mix}
550 (enthalpy of mixing), ΔS_{mix} (entropy of mixing), δ (atomic size difference), and T_{m} are
551 defined as follows[11,54]

552 $$\Delta H_{\mathrm{mix}} = \sum_{i=1,\, i\neq j}^{n} \Omega_{ij} c_i c_j = \sum_{i=1,\, i\neq j}^{n} 4\Delta H_{ij}^{\mathrm{mix}} c_i c_j \quad (1)$$

553 $$\Delta S_{\mathrm{mix}} = -R \sum_{i=1}^{n} c_i \ln c_i \,, = \sum_{i=1}^{n} c_i = 1 \quad (2)$$

554 $$\delta = \sqrt{\sum_{i=1}^{n} c_i (1 - r_{\mathrm{i}}/\bar{r})^2}, \bar{r} = \sum_{i=1}^{n} c_i \, r_{\mathrm{i}} \quad (3)$$

555 $$T_{\mathrm{m}} = \sum_{i=1}^{n} c_i \, (T_{\mathrm{m}})_i \quad (4)$$

556 where $(T_{\mathrm{m}})_i$ is the melting point of the ith component and R represents the gas
557 constant ($8.314\ \mathrm{J \cdot K^{-1} \cdot mol^{-1}}$); $\Delta H_{ij}^{\mathrm{mix}}$ is the enthalpy of mixing of the ith and jth
558 components based on the Miedema macroscopic model[55]. In addition, c_{i} and c_{i} are the
559 atomic percentages of the ith and jth constituent elements, respectively; and r_{i}
560 indicates the atomic radius of the ith component[11]. On this basis, we developed three
561 MESSs with different Ti/Al contents, i.e., Ti_4Al_3, Ti_6Al_5, and Ti_7Al_7. Then we first
562 calculated equilibrium phases of the three MESSs above, as shown in Extended Data
563 Figs. 1a, b, and c. The calculations of phase equilibria were performed with JMatPro
564 (www.sentesoftware.co.uk), which can be used to guide the subsequent heat-treatment
565 process.

566 Based on the calculation results, the homogenization and recrystallization
567 temperatures should be controlled below 1,200 °C, above which the alloys start to
568 melt. In addition, it is noted that the volume fraction of the harmful $L2_1$ phase
569 decreases with the temperature in the high-temperature range of ~ 800 - 1,200 °C, and

570 thus, the homogenization and recrystallization temperatures selected should be as
571 close to 1,200 °C as possible. Below 800 - 900 °C, the favorable $L1_2$ phase is in
572 equilibrium with the FCC matrix phase, and its volume fraction increases with
573 decreasing temperature, while the harmful $L2_1$ phase is found to decrease with
574 decreasing temperature. However, undesired NiAl or η phases also tend to form at
575 low temperatures, especially for the alloy with a high Ti/Al content (i.e., Ti_7Al_7)
576 wherein the volume fraction of the NiAl phase would increase with decreasing
577 temperature. By weighing the favorable $L1_2$ and other undesired phases, the aging
578 temperature was prudently selected around 600 °C. It is also worth noting that the
579 formation of the $L1_2$ phase is generally accompanied by the precipitation of σ and
580 BCC complex phases, whereas neither of them has been observed experimentally,
581 probably due to the incoherence of the precipitates/matrix interfaces and the
582 corresponding large nucleation barrier.

583 Through the above analysis, we selected a homogenization and recrystallization
584 temperature of 1,150 °C and a preliminary aging temperature range of 550 - 650 °C.
585 The optimal aging temperature was selected to be 600 °C, which was determined by
586 comparing the mechanical properties of alloys aged at different temperatures (550 -
587 650 °C). The tensile properties of the three alloys with different Ti/Al contents
588 prepared by the above optimized heat-treatment processes are shown in the Extended
589 Data Figure 1d. In order to avoid discrepancies between the actual and nominal
590 compositions, we simultaneously performed mechanical-performance tests on two
591 other alloys with a similar composition to Ti_6Al_5, i.e., Ti_6Al_6 and Ti_5Al_5, which are

592 produced by the same heat-treatment processes. As can be seen from the Extended
593 Data Fig. 1d, the Ti_6Al_5 alloy exhibits the best synergy of strength and ductility
594 among the five MESSs. Finally, combining the thermodynamics approach with the
595 experimental screening, we successfully determined an optimum chemical
596 composition of our Co-free MESS, i.e., $Fe_{47}Cr_{16}Ni_{26}Ti_6Al_5$ (at. %), which contains a
597 large number of ordered coherent $L1_2$-type Ni_3(Ti, Al) NPs in the FCC-structured
598 FeCrNi base alloy.

599 **Materials preparation.** Two alloys, $Fe_{47}Cr_{16}Ni_{26}Ti_6Al_5$ and $Fe_{47}Cr_{16}Ni_{26}$ (at. %),
600 were fabricated by arc melting pure elements under a Ti-gettered high-purity argon
601 atmosphere. The starting elemental materials were at least 99.99 wt. % pure. All the
602 alloy ingots were repeatedly melted for at least six times to ensure a chemical
603 homogeneity, and finally drop-cast into a 60 mm × 20 mm × 5 mm copper mold. The
604 ingots were homogenized at 1,150 °C for 2 h, water-quenched to RT, and cold rolled
605 with a total reduction of 70% at RT. The cold-rolled sheets were recrystallized at
606 1,150 °C for about 1 min., and then furnace-cooled to ambient temperature. Finally,
607 the sheets were aged at 600 °C for 1 h and then cooled to ambient temperature by
608 quenching into water. Some specimens were further heat treated at 700 °C for 200 h to
609 evaluate the microstructural stability. The heating rate of the above heat treatments is
610 2 °C min^{-1}, and all the above heat treatment processes were carried out under a
611 vacuum condition (less than 0.001 MPa). The specimens for subsequent tests were cut
612 by electrical discharge machining.

613 **Comparison of raw material cost.** The alloys' cost was estimated using the

price of a pure element, which is available at www.shfe.com.cn. Thus, the estimated cost may be different from the market price.

Microstructural characterization. The matrix grains and fracture morphologies of specimens were examined, using a scanning electron microscope (SEM) and electron backscatter diffraction (EBSD, FEI helios G4 CX). The microstructures of specimens were characterized by employing a transmission electronic microscope (TEM, FEI Talos F200X), which was operated at 200 kV and equipped with energy dispersive spectroscopy (EDS). The NPs were further characterized by an aberration-corrected TEM (FEI Themis Z) operated at 300 kV. Specimens for the EBSD and TEM observations were made by first mechanically grinding to a thickness of ~ 50 μm via SiC papers, then punching into discs with a diameter of 3 mm, and finally electropolishing in an electrolytic solution containing 10 volume percent (vol. %) perchloric acid and 90 vol. % alcohol under a voltage of 26 V. X-ray diffraction (XRD) examination was carried out on a Rigaku D/max-2500/PC X-ray diffractometer with Cu-Kα radiation (λ = 0.154 nm). The θ - 2θ scanning was conducted in the range of 30^{o} - 100^{o} with a scanning speed of 2^{o} min^{-1}. Three-dimensional atom probe tomography (3D-APT) was performed in a CAMECA Instruments LEAP 5000XR local electrode atom probe. The specimens were analyzed in a voltage mode, at a specimen temperature of 50 K, a pulse repetition rate of 200 kHz, a pulse fraction of 0.2, and an ion collection rate of 0.5% ions per field-evaporation pulse. Needle-shaped specimens required for APT were fabricated by lift-outs and annular milling in an FEI Scios focused ion beam/scanning

electron microscope (FIB/SEM). Imago Visualization and Analysis Software version 3.8.10 (www.atomprobe.com) was employed for three-dimensional reconstructions and data analysis. The obtained compositions were used to evaluate the volume fractions of the FCC and $L1_2$ phases, using the level rule. The equation[16] can be described as: $f^{L1_2} = (c_i^{nominal} - c_i^{matrix})/(c_i^{precipitate} - c_i^{matrix})$, where $c_i^{nominal}$, c_i^{matrix}, and $c_i^{precipitate}$ refer to the atomic ratio of each element, *i*, in the nominal alloy composition, FCC matrix, and $L1_2$ phases, respectively. Bring the atomic ratio for each elemental to the above equation, respectively, then fitting the all points to a linear relationship yields a slope, which is equal to the volume fraction of the $L1_2$ NPs.

Mechanical tests. Flat dog bone-shaped tensile and creep specimens with a gauge length of 5 mm and a cross-section area of 1.8 mm × 1.5 mm were cut by electrical discharge machining and polished with 2,000-grit SiC papers. A computer-controlled WDW-50S MTS testing machine was employed to investigate the tensile properties. All tensile tests were conducted at a nominal strain rate of 0.001 s^{-1}. For high-temperature tensile tests, specimens were first heated to the desired testing temperatures at a rate of 40 °C min^{-1} and then remained at the testing temperatures for 5 min. before tensile tests. Each sample was tested three times to ensure repeatability. The tensile-loading direction was parallel to the rolling direction. A contactless strain gauge based on a digital image correlation (DIC) technique with a high accuracy of 6 μm was designed to instantaneously capture and analyze the strain images. The DIC technique, which correlates the speckle pattern between images, can numerically evaluate the strain distribution and calculate the axial strain of the tensile specimens.

The strain field was analyzed, employing a MERCURY software (www.testingequipmentie.com). The necking point and the uniform elongation were determined by the point of a maximum load. The work-hardening rate, θ, was derived by differentiating the true stress, σ_t, over the true strain, ε_t, using the equation, $\theta = d\sigma_t/d\varepsilon_t$. Tensile creep tests were performed in a uniaxial tensile mode on an RDL-50 testing machine at 750 ^oC under different applied stresses ranging from 70 to 300 MPa in air. The creep strain was measured continuously, using a grating transducer extensometer with a displacement resolution of ± 1 μm. The steady-state creep rate was determined by linearly fitting the creep strain versus time curve in the steady-state creep stage.

Neutron diffraction. Neutron diffraction was performed on the engineering materials diffractometer, VULCAN, at the Spallation Neutron Source, Oak Ridge National Laboratory. A high-resolution neutron-diffraction mode with a d-spacing coverage of 0.5 - 3.5 Å was used to measure the undeformed MESS sample. Rietveld refinement was performed, using GSAS with EXPGUI. The MESS samples underwent tensile tests at RT and 600 ^oC were subjected to in-situ neutron diffraction with a high-intensity mode. The FCC and $L1_2$ structures were used to refine the lattice parameters (a_{FCC} = 0.3606 nm, and a_{L12} = 0.3611 nm), phase fraction (f_{L12} = 17.3%), and lattice mismatch (0.124%) by Rietveld refinement. The full width at half-maximum (FWHM) for $L1_2$'s {210} and {211} diffraction peaks was used for quantifying deformability, which was obtained through correcting the instrumental broadening with a near-perfect (broadening-free) Si sample.

Estimation of strengthening by various mechanisms. The RT yield strength (σ_y) of our MESS is estimated based on the individual strengthening contribution, expressed as[47]

$$\sigma_y = \sigma_0 + \sigma_s + \sigma_g + \sigma_d + \sigma_p \quad (5)$$

where σ_0 is the intrinsic strength, or the so-called lattice-friction strength, σ_s is the solid-solution strengthening, σ_g is the grain-boundary strengthening, σ_d is the dislocation strengthening, and σ_p is the precipitation strengthening. Here, the intrinsic lattice friction stress (165 ± 5 MPa) of the base $Fe_{47}Cr_{16}Ni_{26}$ alloy is used.

The present MESS can be simply treated as a FeCrNi-solvent matrix containing Ti and Al solutes, and a standard model for substitutional solid-solution strengthening, based on dislocation-solute elastic interactions, can be directly applied to evaluate the solution strengthening term, σ_s, caused by Ti and Al[47,56]

$$\sigma_s = MG\varepsilon_s^{1.5}c^{0.5}/700 \quad (6)$$

where G is the shear modulus for the MESS (81 GPa)[2], c is the total molar ratio of Ti + Al in the simple FCC matrix (Extended Data Table 1), and M = 3.06 is the Taylor factor. The strength increment caused by solid-solution hardening, σ_s, is calculated to be = 22 ± 2 MPa.

The grain-boundary strengthening contribution, σ_g, is estimated on the basis of the Hall-Petch relation[16,47]:

$$\sigma_g = k_y (d_a^{-0.5} - d_c^{-0.5}) \quad (7)$$

where d_a and d_c represent the grain size of the aged and as-cast MESS, respectively. Using the value of k_y (966 ± 25 MPa $\mu m^{0.5}$) derived from the FeCrNi system[57] and the

grain sizes (d_a = 70 μm and d_c = 249 μm) measured by EBSD. One obtains σ_g = 54 ± 1 MPa.

The strengthening contribution from dislocations (σ_d) is calculated according to the Taylor-hardening law[28]

$$\sigma_d = M\alpha G b \rho^{0.5} \quad (8)$$

where α is a constant (0.2), b is the magnitude of the Burgers' vector, and ρ is the dislocation density. Here, $b = \sqrt{2}/2a_{MESS}$, and the lattice parameter, a_{MESS}, is 0.3607 nm (measured from neutron diffraction). The dislocation density (ρ) is calculated by the expression of $\rho = \sqrt{2}\varepsilon/(2db)$, where ε (0.104%) is the microstrain estimated from the XRD result, using the well-known Williamson-Hall method[58], d is the average grain size. Hence, $\rho = 1.88 \times 10^{13}$ m^{-2}. Therefore, σ_d is 57 ± 33 MPa.

For an alloy containing high-density NPs, the precipitation hardening, σ_p, is primarily responsible for the pronounced increase in the yield strength[52, 53]. In the present MESS, the coherent NPs are significantly sheared by dislocations after yielding (Fig. 4d). In this case, three contributing factors are considered for the yield strength, i.e., the particle-matrix coherency strengthening (σ_{cs}), modulus-mismatch strengthening (σ_{ms}), and atomic-ordering strengthening (σ_{os})[28,47,59], which can be, respectively, estimated by

$$\sigma_{cs} = M\alpha_{\varepsilon}(G\varepsilon)^{1.5}[rf/(0.5Gb)]^{0.5} \quad (9)$$

$$\sigma_{ms} = 0.0055M(\Delta G)^{1.5}(2f/G)^{0.5}(r/b)^{3m/2-1} \quad (10)$$

$$\sigma_{os} = 0.81M[\gamma_{APB}/(2b)](3\pi f/8)^{0.5} \quad (11)$$

where α_{ε} = 2.6 for the FCC structure, m = 0.85, $\varepsilon \approx 3\Delta a/a$ is the constrained

lattice-parameter mismatch, with $\Delta a/a$ = 0.0014 in the present work, where Δa is the difference of lattice constants between the NPs and the FCC matrix calculated from the neutron-diffraction results; ΔG is the shear-modulus mismatch between the NP's and matrix, ΔG = 4 GPa[47], r is the radius (7.2 nm), and f is the volume fraction (~ 0.17) of the NPs. γ_{APB} is the antiphase boundary (APB) energy of the NPs, which is strongly dependent on the Ti/Al ratio of the NPs and can be estimated to be about 0.206 $J \cdot m^{-2}$ [36]. The estimated strengthening contributions from the order strengthening, coherency strengthening, and modulus-mismatch strengthening are 444, 106, and 21 MPa, respectively. The first two (σ_{cs} and σ_{ms}) occur before dislocations shear precipitates, while the latter (σ_{os}) takes place during shearing. In this case, the larger one between ($\sigma_{cs} + \sigma_{ms}$) and σ_{os} determines the total strength increment of the shear mechanism[47]. Thus, the overall precipitation strengthening from the NPs is ~ 444 ± 32 MPa [σ_{cs} (106 MPa) + σ_{ms} (21 MPa) = 127 MPa; and σ_{os} = 444 MPa].

The estimated σ_y of the MESS is 742 ± 66 MPa. It is apparent that the precipitation strengthening from the NPs offers the largest contribution (~ 60%) to the yield strength of the MESS. Note that further increasing the Ti/Al addition (the Extended Data Fig. 1) - which may increase the number density of NPs - would continue to increase the strength of the MESS, but inevitably at the cost of ductility. Thus, the content of Ti/Al should be tailored to achieve the best combination of strength and ductility. In addition, it is noted that the estimated σ_y differs from the experimental value (927 MPa) to some extent. First, several intrinsic parameters (e.g., ΔG, k_y, and G) are taken from other alloys in our calculations. Second, the strength

746 contribution from the $L2_1$ phase at the grain boundaries is neglected. In addition, there
747 may be some errors in data fittings, statistical values, and elemental content
748 determinations. Nonetheless, in any case, the precipitation strengthening from the
749 high-density coherent $L1_2$ NPs dominates the overall strength of the MESS.

750 **Data availability**

751 The data that support the findings of this study are available from the corresponding
752 authors upon reasonable request.

753 51. Viswanathan, G. B. *et al.* Precipitation of ordered phases in metallic solid solutions: A
754 synergistic clustering and ordering process. *Scr. Mater.* **65**, 485-488 (2011).

755 52. Booth-Morrison, C. *et al.* Effects of solute concentrations on kinetic pathways in Ni–Al–Cr
756 alloys. *Acta. Mater.* **56**, 3422-3438 (2008).

757 53. Lu, K. Stabilizing nanostructures in metals using grain and twin boundary architectures. *Nat.*
758 *Rev. Mater.* **1** (2016).

759 54. Fu, Z. *et al.* A high-entropy alloy with hierarchical nanoprecipitates and ultrahigh strength. *Sci.*
760 *Adv.* **4**, eaat8712 (2018).

761 55. Takeuchi, A. & Inoue, A. Classification of bulk metallic glasses by atomic size difference, heat
762 of mixing and period of constituent elements and its application to characterization of the main
763 alloying element. *Mater. Trans.* **46**, 2817-2829 (2005).

764 56. Schuh, C. A., Nieh, T. G. & Iwasaki, H. The effect of solid solution W additions on the
765 mechanical properties of nanocrystalline Ni. *Acta. Mater.* **51**, 431-443 (2003).

766 57. Zhang, C. *et al.* Effect of aging temperature on the precipitation behavior and mechanical
767 properties of Fe-Cr-Ni maraging stainless steel. *Mater. Sci. Eng. A* **806** (2021).

58. Williamson, G. K. & Hall, W. H. X-ray line broadening from filed aluminium and wolfram. *Acta. Metall.* **1**, 22-31 (1953).

59. Ardell, A. J. Precipitation hardening. *Metall. Trans. A* **16**, 2131-2165 (1985).

Acknowledgements

The present work was financially supported by the National Natural Science Foundation of China (Nos. 51971195 and 11935004), the Natural Science Foundation of Hebei Province (No. B2020203037), the Youth Fund Project of Science and Technology Research of Hebei Province (No. QN2020210). P.K.L. appreciates the supports from (1) the National Science Foundation (DMR-1611180, 1809640, and 2226508) and (2) the US Army Research Office (W911NF-13–1-0438 and W911NF-19–2-0049). R.F. thanks for the support from the Materials and Engineering Initiative at the Spallation Neutron Source (SNS), Oak Ridge National Laboratory (ORNL). A portion of the current research used resources at SNS, a U.S. Department of Energy (DOE) Office of Science User Facility operated by the ORNL. The authors would like to thank Dr. Dunji Yu for his assistance in neutron diffraction experiments, and Dr. Zuohua Wang and Dr. Tingting Yang for their assistance in the TEM characterization.

Author contributions

T.S., K.W., and X.C. designed the study. B.S., S.X., Z.B., and T.S. supervised K.W., F.M., C.D., and S.D. for the synthesis of specimens and the characterization of microstructures and mechanical properties. K.W. and F.M. conducted XRD, EBSD, and mechanical-property tests. K.W, C.D., and S.D. performed TEM observations and

analyses. H.Z., and Y.W. conducted correlative 3D-ATP. K.W., X.C., T.S., and P.L. analyzed the data and discussed the results. R.F. and K.A. performed the in situ neutron-diffraction experiments and analyzed the resultant data. K.W., X.C., R.F., P.L., and T.S. wrote the manuscript. All authors discussed the results and commented on the manuscript.

Competing interests: The authors declare no competing interests.

Additional information

Supplementary information is available for this paper.

Correspondence and requests for materials should be addressed to Baoru Sun, Peter K. Liaw, or Tongde Shen.

Reprints and permissions information is available at www.nature.com/reprints.

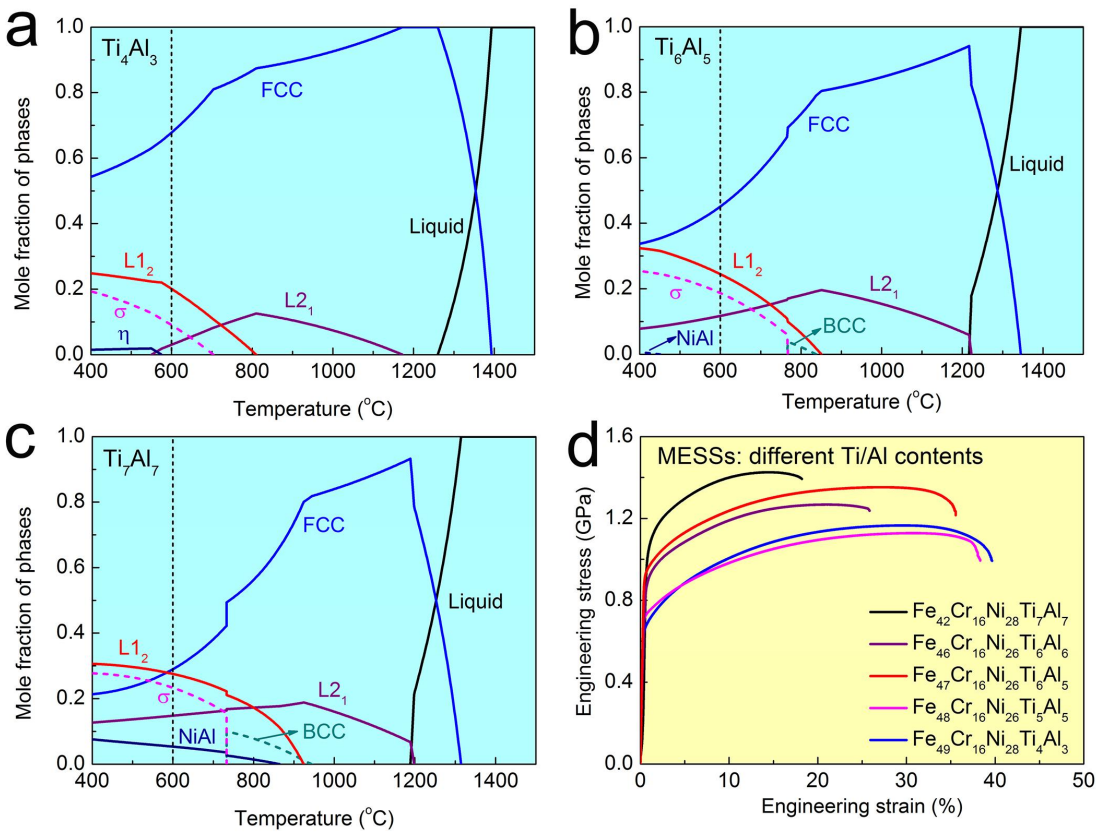

808 **Extended Data Fig. 1 | a - c** Equilibrium phase diagrams calculated by the JMatPro software for

809 MESSs with different compositions, Ti_4Al_3 (**a**), Ti_6Al_5 (**b**), and Ti_7Al_7 (**c**). **d** Tensile curves of

810 alloys with different Ti/Al contents.

811

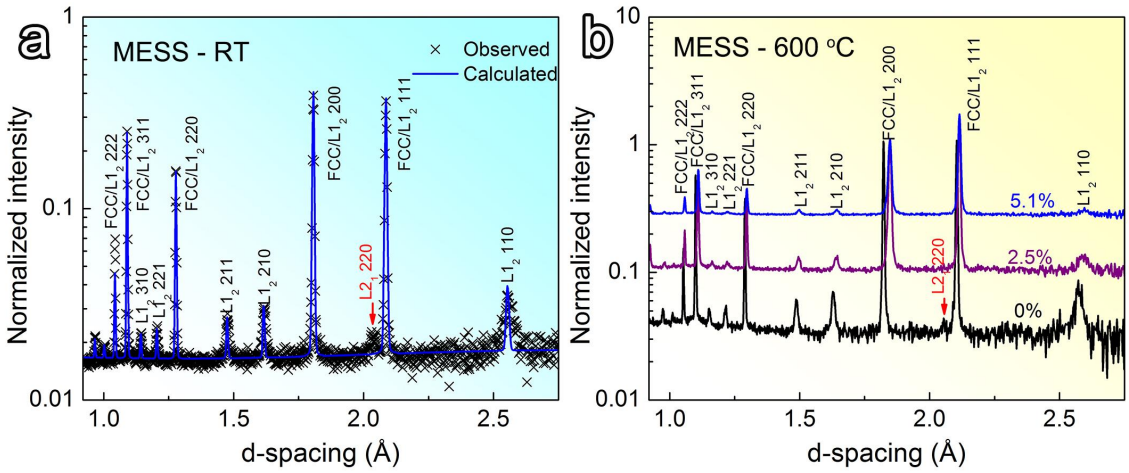

812 **Extended Data Fig. 2 | a** High-resolution neutron-diffraction pattern of the undeformed MESS at
813 RT, showing the co-existence of the FCC matrix (α_{FCC} = 0.3606 nm) and L1$_2$ phase (α_{L12} = 0.3611
814 nm) with a lattice mismatch of 0.124%. Black crosses indicating experimental observations, red
815 lines representing the calculated fit by Rietveld refinement. **b** Neutron-diffraction patterns at
816 selected tensile strains and at 600 °C, suggesting that no other phases form during tensile
817 deformation.
818

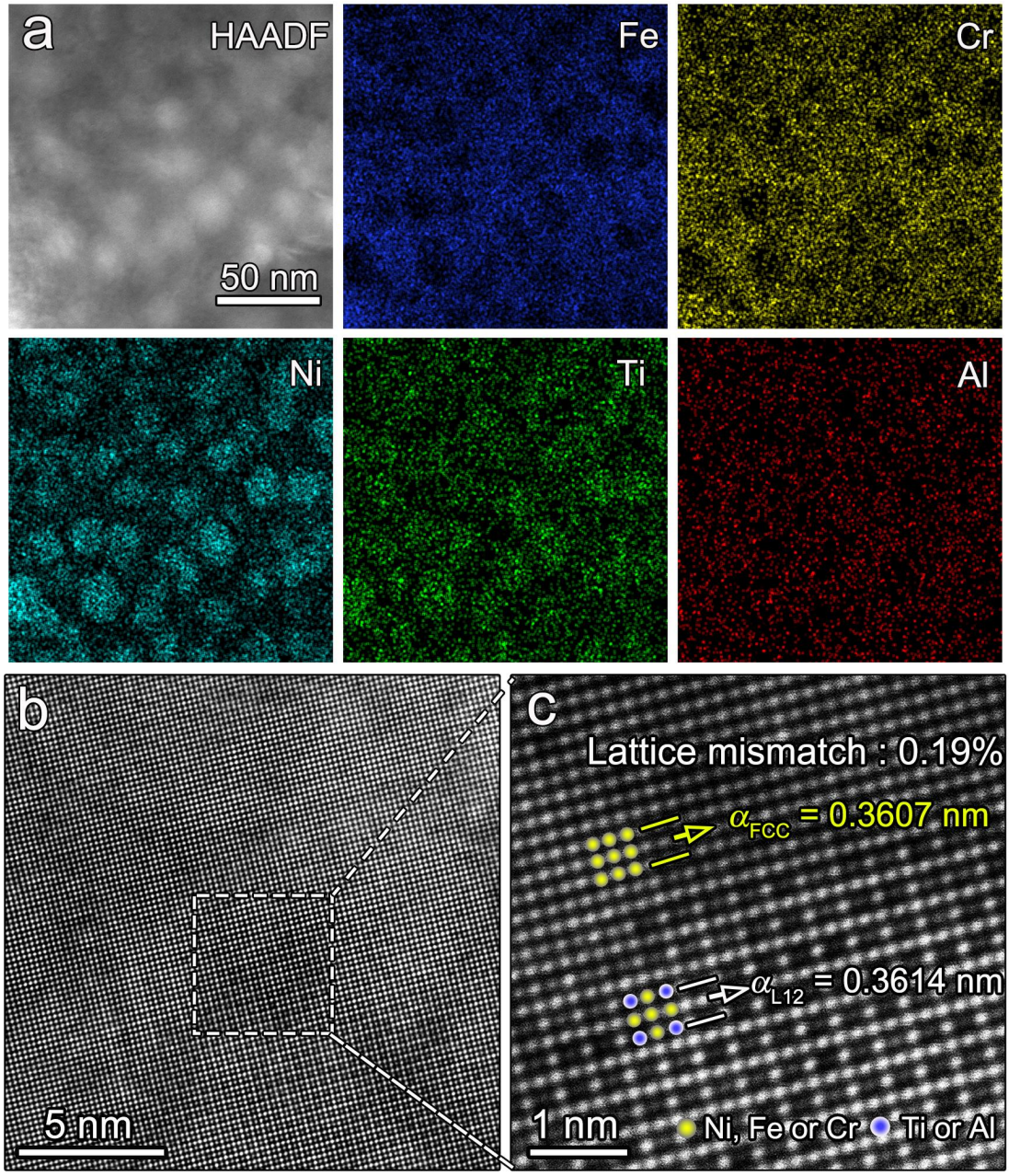

819 **Extended Data Fig. 3 | a** HAADF image and STEM-EDS mappings of the MESS. The elemental
820 mappings illustrating that Fe and Cr partition to the FCC matrix, and Ni and Ti partition to the $L1_2$
821 phase. **b** Atomic-resolution HAADF-STEM image taken from the [001] zone axis exhibiting a
822 coherent interface between the $L1_2$ NP and FCC matrix. **c** A close-up view of the region marked
823 by the white dashed rectangle in **b** revealing the sublattice occupations of different elements in the
824 $L1_2$ NP and FCC matrix.
825

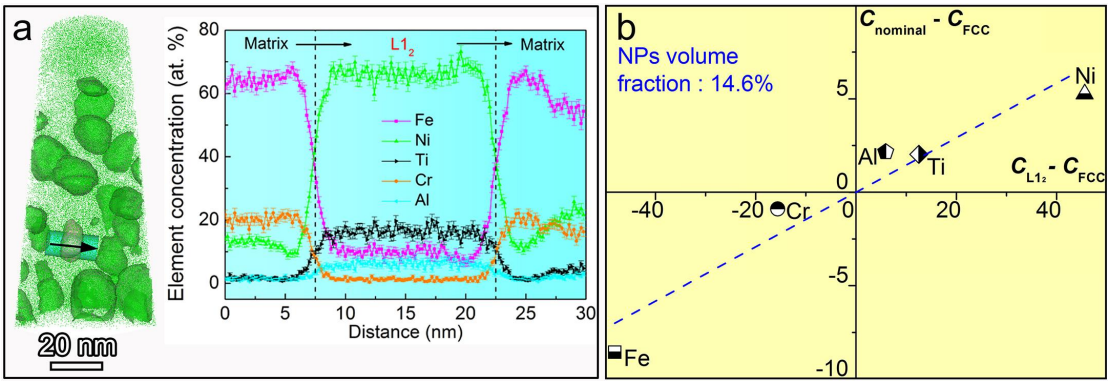

826 **Extended Data Fig. 4 | a** One-dimensional concentration profiles from the APT results showing
827 the elemental distributions. **b** Lever-rule diagram of the chemical composition of the MESS
828 obtained from Fig. 2b indicating the volume fraction of the $L1_2$ NPs in the MESS through the
829 slope of the line.
830

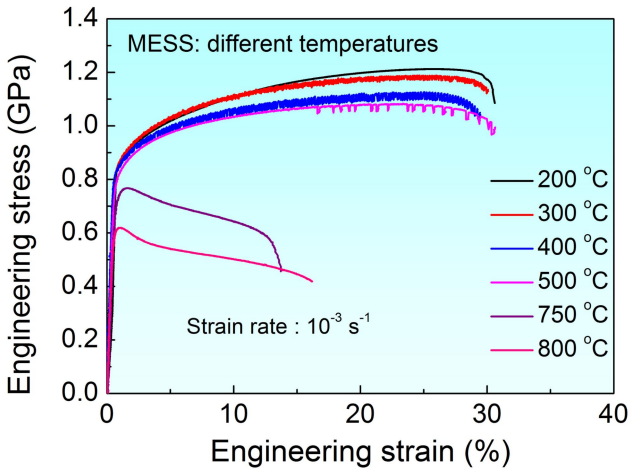

831 **Extended Data Fig. 5** | Uniaxial tensile stress-strain curves of the MESS at elevated

832 temperatures.

833

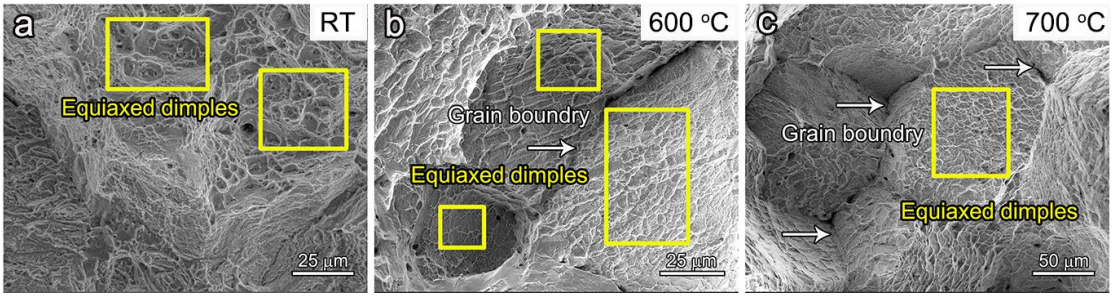

834 **Extended Data Fig. 6 |** SEM micrographs of the fracture surface of the MESS deformed at RT (**a**),

835 600 °C (**b**), and 700 °C (**c**). Jagged lines on the fracture surfaces of 600 °C and 700 °C (especially

836 700 °C) clearly indicating that the sample fractured in an intergranular manner, i.e., along the grain

837 boundaries.

838

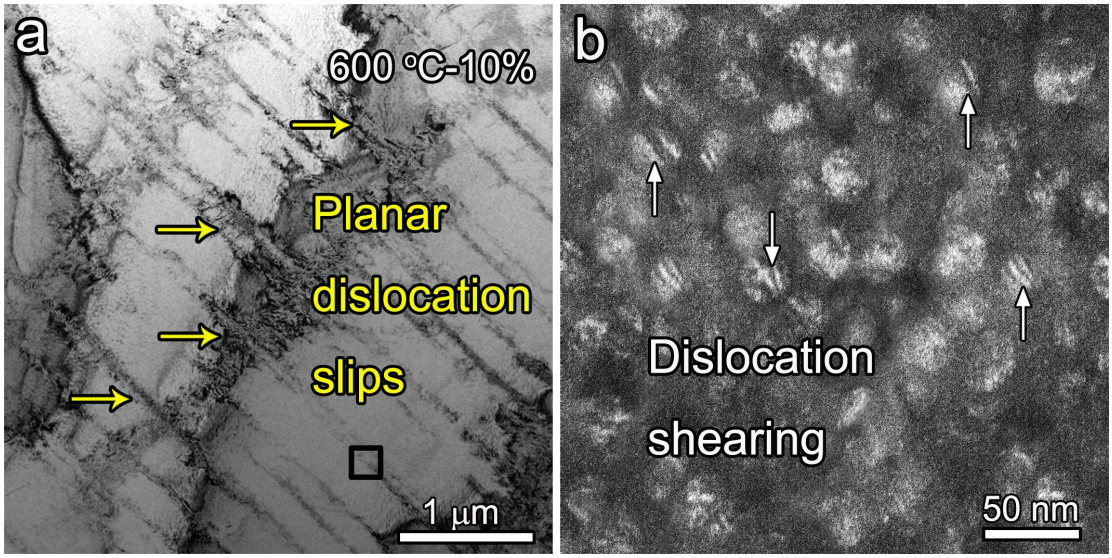

839 **Extended Data Fig. 7 | a** Deformation microstructures of the 10%-strained sample at 600 °C

840 showing prevalent planar-dislocation slips on the {111} planes. **b** A close-up view of the region

841 marked by the black rectangle in **a** revealing dislocations shearing through $L1_2$ NPs.

842

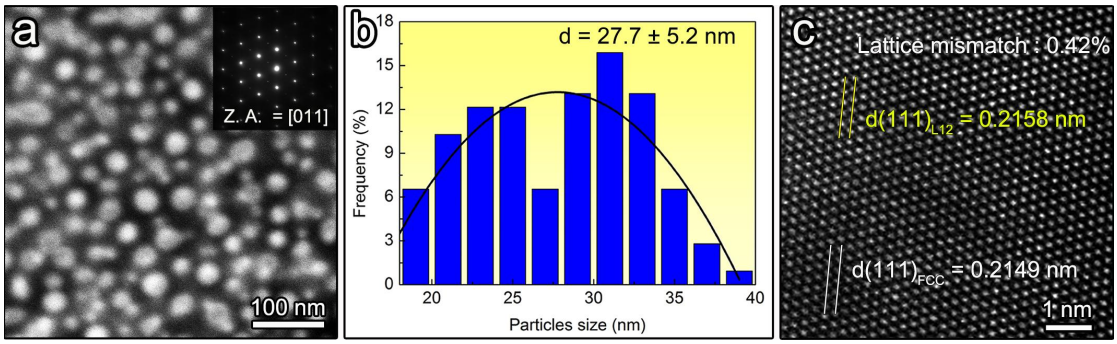

843 **Extended Data Fig. 8 |** NPs of the MESS annealed at 700 °C for 200 h. **a** HAADF-TEM image.

844 Inset showing the corresponding SAED pattern. **b** Statistical distributions of the particle sizes. **c**

845 High-resolution-TEM (HRTEM) image illustrating the interfacial coherency of the FCC

846 matrix/$L1_2$ NP after ageing at 700 °C for 200 h, $d(111)_{L12}$= 0.2158 nm, and $d(111)_{FCC}$ = 0.2149 nm,

847 resulting in a small lattice mismatch of 0.42%.

848

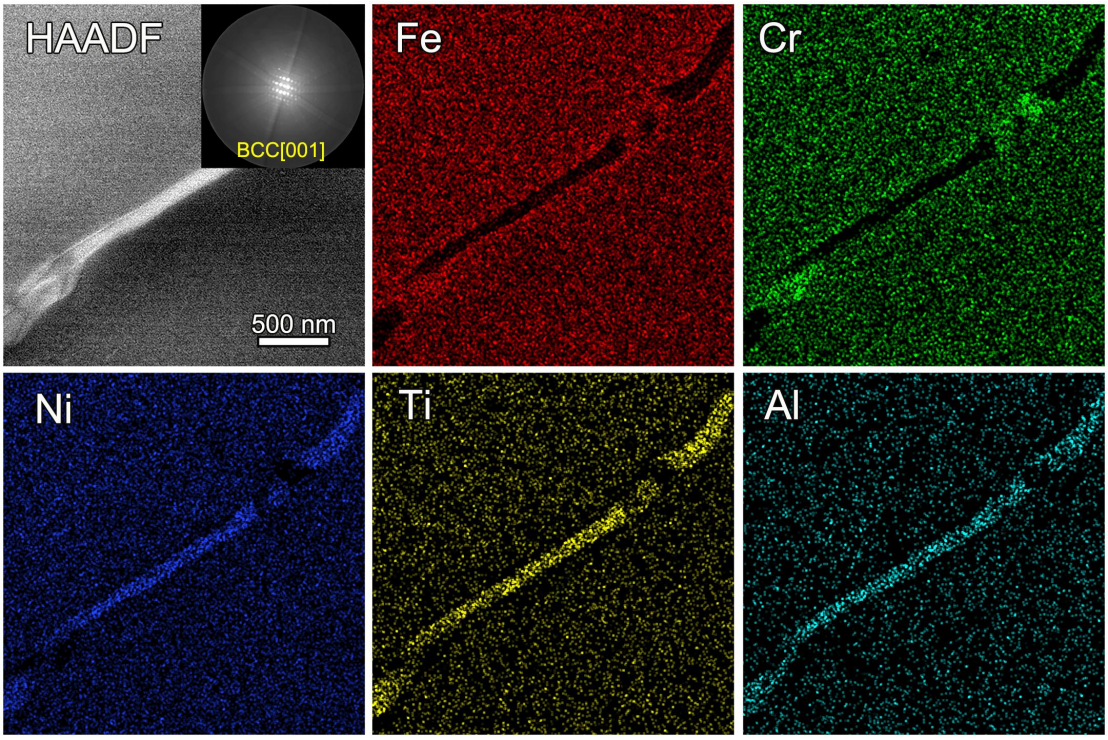

849 **Extended Data Fig. 9 |** Microstructural characterization of the grain-boundary $L2_1$ phase.

850 Elemental mappings illustrating that Ni, Al, and Ti partition to the $L2_1$ phase. Inset in the HAADF

851 image showing the indexed convergent beam electron-diffraction pattern of the $L2_1$ phase with a

852 BCC structure.

853

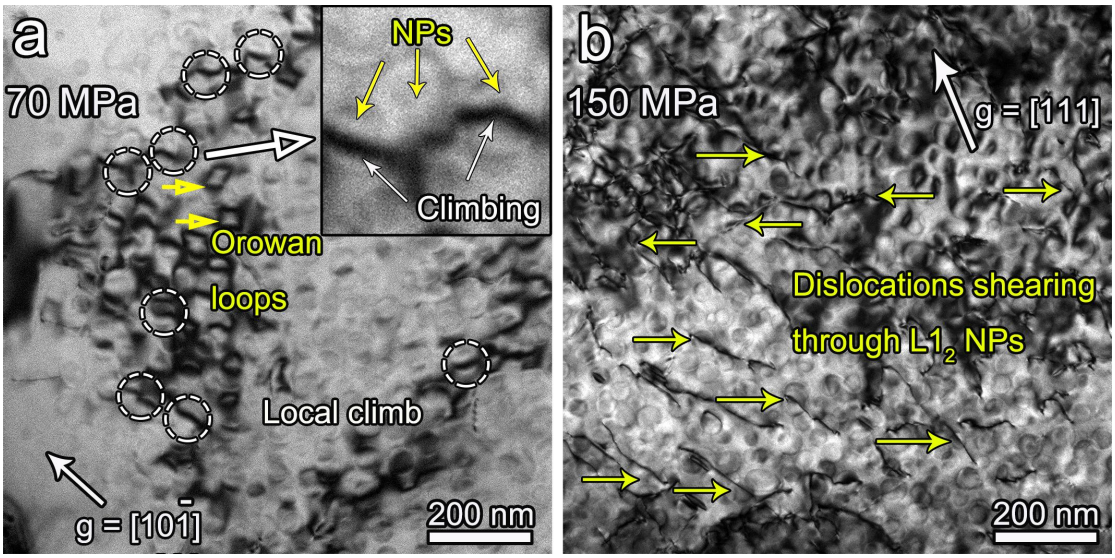

854 **Extended Data Fig. 10** | TEM characterization of the deformation microstructures of the
855 creep-strained specimens. **a** BF-TEM image of the alloy crept at 750 °C/70 MPa for 300 h, most
856 of dislocations being strongly curved. Inset showing the detailed interactions where a sliding
857 dislocation is climbing up the encountered $L1_2$ NPs. **b** BF-TEM image of the alloy crept at 750
858 °C/150 MPa for 128 h, prevalent dislocations shearing through $L1_2$ NPs (yellow arrows).
859

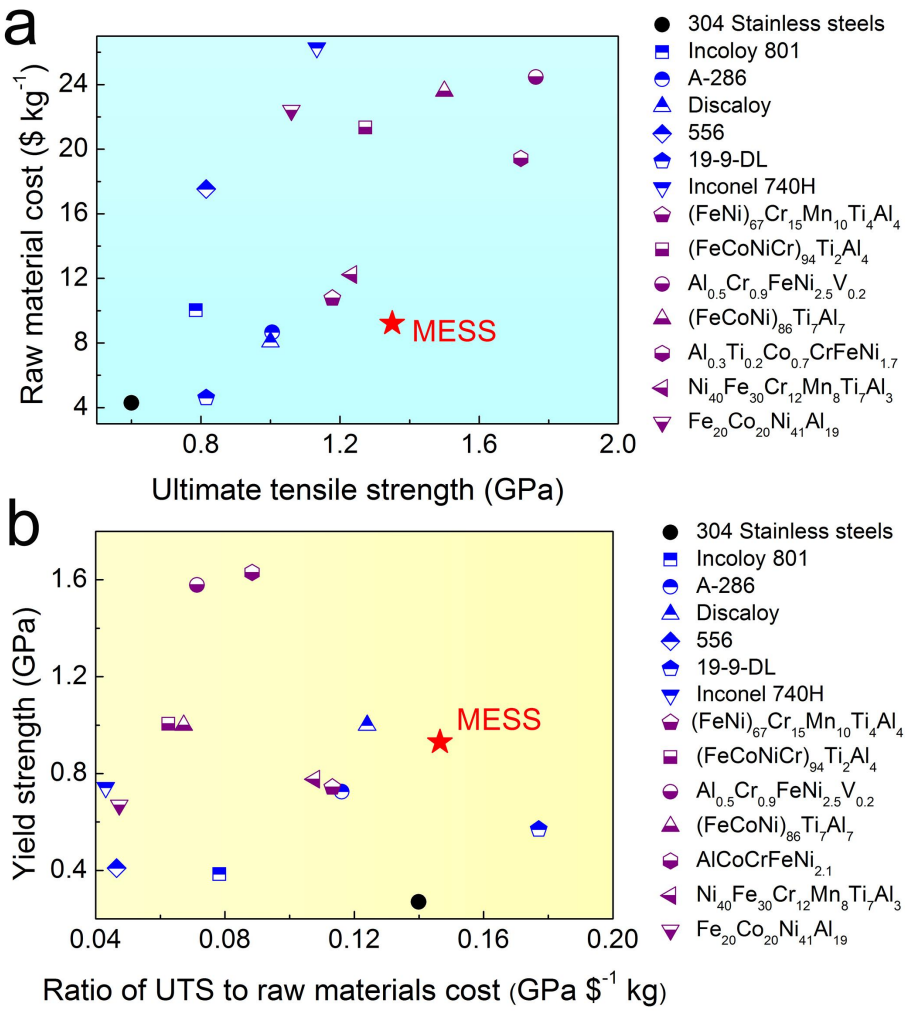

860 **Extended Data Fig. 11 | a** Comparison between the ultimate tensile strength and raw material cost
861 for typical 304 austenitic stainless steels, Fe-based superalloys, some recently reported
862 HEAs/MEAs, and the present MESS. **b** Comparison between the yield strength and ratio of the
863 ultimate tensile strength (UTS) to raw material cost for typical 304 austenitic-stainless steels,
864 Fe-based superalloys, some recently reported HEAs/MEAs, and the present MESS.
865

Extended Data Table 1 | Chemical compositions of the FCC matrix and $L1_2$ phase in the MESS characterized by the 3D-APT measurement.

Phase	Chemical composition (atomic percent, at. %)				
	Fe	Cr	Ni	Ti	Al
Matrix	55.6 ± 0.5	16.9 ± 0.4	20.7 ± 0.4	4.0 ± 0.2	2.6 ± 0.2
$L1_2$	7.4 ± 0.8	1.3 ± 0.3	66.0 ± 2.2	16.5 ± 1.6	8.8 ± 0.9